Utilizing Room Temperature Liquid Metals for Mechanically Robust Silicon Anodes in Lithium-Ion Batteries

Author

Hapuarachchi, Sashini NS, Nerkar, Jawahar Y, Wasalathilake, Kimal C, Chen, Hao, Zhang, Shanqing, O'Mullane, Anthony P, Yan, Cheng

Published

2018

Journal Title

Batteries and Supercaps

Version

Accepted Manuscript (AM)

DOI

10.1002/batt.201800047

Utilising Room Temperature Liquid Metals for Mechanically Robust Si Anodes in Li-ion Batteries

Sashini N. S. Hapuarachchi, Jawahar Y. Nerkar, Kimal Chandula Wasalathilake, Hao Chen, Shanqing Zhang, Anthony P. O'Mullane and Cheng Yan *

S. N. S. Hapuarachchi, K.C. Wasalathilake, Prof. A. P. O'Mullane, Prof. C. Yan
School of Chemistry, Physics and Mechanical Engineering, Queensland University of Technology (QUT), Brisbane, QLD 4001, Australia.
E-mail: c2.yan@qut.edu.au
Dr J. Y. Nerkar
Institute for Future Environments, Queensland University of Technology (QUT), Brisbane, QLD 4001 Australia
H. Chen, Prof. S. Zhang
Centre for Clean Environment and Energy, Environmental Futures Research Institute and Griffith School of Environment, Gold Coast Campus, Griffith University, QLD 4222, Australia

Keywords: Si, liquid metal, crack-healing, Li-ion batteries

Silicon has attracted attention as one of the most promising anode materials for future generation energy storage devices, owing to its high theoretical specific capacity. However, its use has been impeded by significant volume expansion during electrochemical lithiation. In this work we utilise liquid galinstan (68.5% Ga, 21.5% In and 10% Sn) to repair the cracking caused by volume expansion in Si thin film and Si composite electrodes. A bridging mechanism is observed, through which the electrical conductivity can be significantly improved. The composite electrode delivers an initial capacity of 2697 $mAhg^{-1}$ and reaches a coulombic efficiency ~100% after 140 cycles. In addition, nanoindentation tests show that a better mechanical behavior is achieved with increased flexibility. We believe that these results may provide a way to prepare mechanically robust high capacity electrodes.

1. Introduction

Even though Li-ion batteries have dominated the energy storage market for over two decades, their current capacity is unable to meet ever increasing requirements for applications in long distance electric vehicles, grid storage of electricity and higher-end portable electronic devices.[1-4] Therefore, development of novel electrode materials to realize high energy density and long cycle life has become an urgent task.[5-8]

Recently, Silicon (Si) has been identified as a promising candidate for Li-ion battery anodes due to its high theoretical capacity of 3579 $mAhg^{-1}$ at room temperature, compared to the limited capacity (372 $mAhg^{-1}$) of conventional graphite anodes.[9-11] Despite the additional advantages such as low operating voltages, environmental friendly and natural abundance, the technical challenge with Si anode is the large volume expansion (~300%) upon lithiation.[12] Repetitive volume expansion/contraction during lithiation/delithiation cycles results in cracking and pulverization of active particles. This causes loss of contact between Si particles and the current collector leading to early capacity decay. [13,14] With limited success, reducing Si particle size to the nanoscale was practiced to overcome this problem.[15-18] On the other hand, use of other materials such as carbon, graphene, polymers and transition metal oxides with Si nanostructures, to create composite electrodes is considered as another strategy to solve this technical problem in Si electrodes.[19-26]

Meanwhile, metal based electrodes such as Li, Sn, Al and Ga have received recognition for their significant electrical conductivity.[15] In principle, liquid metals such as Galinstan (68.5% Ga, 21.5% In and 10% Sn) have a great potential as electrode materials given Ga, In and Sn have high theoretical specific capacities of 769, 1012 and 960 $mAhg^{-1}$ respectively.[27] Due to their liquid nature, it is expected low melting point liquid metals are able to heal the cracks created by volume expansion and improve the electrical conductivity. A liquid metal electrode of Ga and Sn demonstrated enhanced cycle performance due to its self-healing ability at room temperature.[28] The theoretical capacity of the Ga and Sn based liquid metal electrode,

however, is much lower than Si. Naturally, a hybrid of Si and liquid metals is considered to be a reasonable choice as electrode materials which should be able to deliver a high capacity when compared to pure liquid metal. However, very limited research has been conducted in this direction. In addition, the possible synergy between the composite approach and incorporation of liquid metals in Si anodes deserves further investigations.

In this work we added liquid metal galinstan to thin film and composite Si electrodes (**Figure 1**) and investigated their electrochemical and mechanical behavior. The benefit of incorporating a liquid metal (LM) is confirmed in both strcutures.

2. Results and Discussion

2.1 Self-Healing Effect of LM on Si Thin Film Electrode

XRD patterns revealed that the as deposited Si thin films are amorphous in nature as the only peaks observed are assigned to the stainless steel substrate (Figure S1). The surface of the as deposited Si thin films appeared to be quite uniform in nature as shown in **Figure 2**a. Figure 2b-f show the surface morphology and elemental mapping of Si/LM thin films obtained by SEM and EDS imaging techniques. The highly spherical nature and absence of extensive wrinkle formation on the surface of the LM droplets can be attributed to low LM oxidation, as all experiments were conducted in an oxygen controlled environment, thereby, decreasing the formation of the surface oxide layer (Figure S2).

Galvanostaic charge/discharge tests were performed on the as prepared Si thin film electrodes to observe the function of LM particles when subjected to electrochemical lithiation and delithiation. Si and LM deposited Si thin film electrodes were discharged to 0.01 V at a current of 90 mAg^{-1} and subjected to post cycling SEM characterization after rinsing the electrodes with DMC to remove any residual Li salt. **Figure 3**a illustrates SEM images obtained for the lithiated Si thin film electrode. It can be observed that the resulting morphology of the lithiated Si electrode is distinctly different from the uniform nature of the pristine Si thin film. Si particles have expanded in volume due to insertion of Li^+ ions into the

Si matrix. Additionally, several cracks are visible on the surface of the Si thin film electrode, created by mechanical stresses built up during volume expansion. Figure 3b depicts the surface morphology of the LM deposited Si thin film after electrochemical lithiation. It is apparent that LM particles have solidified during lithiation, resulting in a rough surface with bumps and ravines as reported in previous work.[28] LM deposited Si thin films were then subjected to a full discharge/charge cycle in order to observe the structure and nature of LM particles after the extraction of Li^+ ions. Figure 3c, d illustrate SEM images obtained for the fully cycled sample where two main observations of the delithiated LM deposited Si thin film electrodes are noted. Firstly, the self-healing ability of the LM particles is revealed as they have recovered their original shape and liquid nature with a smoother surface as opposed to the rough surface of the lithiated electrode. The high surface tension of delithiated LM particles have driven them back to their spherical shape on the Si thin film. Secondly, it can be observed that the LM particles have the ability to bridge the gaps which are created in the Si electrode due to crack formation as a result of extreme volume variation during electrochemical cycling. The capability of LM particles to attach to the Si particles during cycling could in principle maintain the electrical conductivity of the Si thin film, thereby, ensuring that the Si particles do not get electrically isolated due to volume expansion. The SEM images show that a crack healing mechanism is possible in Si thin film electrodes by utilising galinstan droplets attached to the Si electrode.

Figure 4 shows the comparison of electrochemical performance results obtained for Si and Si/LM thin films when cycled at a charge-discharge current of 90 mAg^{-1}. It can be observed that the LM deposited electrode delivered a more stable capacity throughout cycling when compared to the pure Si thin film electrode. After 90 cycles the Si/LM electrode retained more than 50% of its reversible capacity, whereas, the pure Si electrode showed a reversible capacity retention of only 5%.The improved stability of the Si/LM thin film can be attributed

to the LM preserving the electrical conductivity of cracked Si electrodes via a crack-healing mechanism as observed in the SEM images (Figure 3 c, d) shown above.

2.2 Si/LM/N-rGO Composite Electrode

Following the improvement in stability of LM deposited Si thin films, LM was then combined with Si nanoparticles and N-doped reduced graphene oxide (N-rGO) to fabricate Si/LM/N-rGO composite electrodes on a Cu current collector. The rGO (reduced graphene oxide) layers embed Si/LM particles in a 3D supporting network preventing aggregation of LM particles which results in a superior structural backbone. Like LM, rGO also assists in increasing the electrical conductivity of the Si electrode, thereby, improving the overall electrochemical performance of the electrode.[29] XRD characterization was performed on the composite active material powder to reveal the crystalline structure of its components, which is presented in Figure S3. The diffraction peaks detected in the XRD pattern at $2\theta = 28.4^{o}$, 47.3, 56.1 and 69.1 correspond to the Si crystal planes of (111), (220), (311) and (400) in the composite material respectively, confirming the crystalline nature of Si particles as opposed to the amorphous nature of Si in the thin film electrodes deposited by PVD.[30-32] The absence of crystalline diffraction peaks for Ga_2O_3 suggests that the oxide layer formed on the LM surface is amorphous in nature or too thin for detection with XRD which is consistent with previous studies.[33,34]

Nanoindentation tests were carried out to evaluate the mechanical properties of the as prepared electrodes. The depth of indentation for the Si and Si/LM/N-rGO electrodes were 655 nm and 847 nm respectively when the maximum force applied was set to 500 μN (**Figure 5**a). Twelve individual indentations were performed on each sample to derive accurate calculation of the reduced modulus and hardness. Figure 5 b, c show the average values obtained for reduced modulus and hardness, respectively. The Si/LM/N-rGO electrode showed lower reduced modulus and hardness which promote the flexibility of the composite. Galinstan has been reported to have a low Young's modulus enabling its use in applications

which undergo high mechanical deformation such as wearable electronics.[35] Furthermore, another study revealed that introduction of GO, results in decreased values for the Young's modulus and hardness as the porosity of the electrode increases, thereby, improving the flexibility of the electrode.[36] The lower values obtained for reduced modulus and hardness for the Si/LM/N-rGO electrode in our study can be attributed to the enhanced flexibility of the electrode which can accommodate extreme volume expansion of Si more effectively.

The Si and Si/LM/N-rGO slurry coated electrodes were subjected to galvanostatic charge/discharge tests to determine the behavior of LM particles during electrochemical cycling. **Figure 6**a depicts the resulting surface morphology of a Si and Si/LM/N-rGO electrode after 3 electrochemical charge/discharge cycles. Severe cracks can be observed in the Si electrode, whereas, LM particles again demonstrate the ability to bridge gaps created in the Si/LM/N-rGO electrode due to extreme volume expansion. EDS mapping of Si and Si/LM of one of the cracks in the Si/LM/N-rGO composite electrode (Figure 6b) show that LM particles are present in the middle, holding the structure together, thereby, maintaining the electrical conductivity which otherwise could have resulted in early electrode failure due to electrical isolation of the Si particles. Furthermore, EDS elemental mapping of another crack (Figure 6c) confirmed the as expected composition of LM particles consisting of Ga, In and Sn. Although Ga, In and Sn also show some volume expansion upon lithiation, their self-healing nature drives LM particles back to their original shape without any crack formation in these droplets. This is the main advantage of the liquid nature of LM at room temperature, as it can regain its structure without any fracture after a few cycles unlike pure Si. Therefore, it can be perceived that the liquid nature along with the high electrical conductivity and self-healing ability of LM, contribute in enhancing the electrode stability of Si/LM/N-rGO compared to pristine Si.

Cyclic voltammetry (CV) experiments were carried out to evaluate the redox behavior of Si-LM/N-rGO composite electrode associated with Li insertion and extraction, respectively.

Figure 7a shows the CV curves of Si/LM/N-rGO electrode versus Li/Li^+ for the first four cycles when scanned at $0.1mVs^{-1}$ in a potential window of 0.01 V to 1.5 V. During the first cathodic scan, an irreversible broad reduction peak around 0.7 V was observed, which can be attributed to the formation of a solid electrolyte interphase (SEI) layer. During subsequent cycles of cathodic scans, lithium alloying can be observed at 0.15 V, 0.73 V, 0.48 V and, 0.66 V for Si, Ga, In and Sn, respectively. During the reverse scan, anodic peaks observed at 0.34 V and 0.5 V for Si, 0.9 V, 0.68 V and 0.87 V for Ga, In and Sn, respectively are mainly related to the dealloying reactions which are consistent with the reported literature.[28,37-39] A gradual increase in the redox currents during the first four cycles is most likely due to the activation process where more active material is utilized with cycling.

EIS measurements were conducted to evaluate the impedance and lithium diffusion properties of the composite Si/LM/N-rGO electrode in comparison with the control-Si electrode. Figure 7b shows the comparison of Nyquist plot for the Si/LM/N-rGO composite and the Si electrodes at OCV prior to any electrochemical cycling. The lower interfacial charge transfer resistance observed for the composite electrode compared to the Si electrode can be attributed to the improved electrical conductivity of the Si/LM/N-rGO composite electrode. Figure S4 depicts EIS measurements obtained for our composite electrode before and after 50 cycles of lithiation/delithiation which shows that the resistance of the cycled electrode has a lower value when compared to the pristine electrode.

Galvanostatic charge/discharge tests were carried out to evaluate the electrochemical performance of the Si/LM/N-rGO composite electrode during electrochemical cycling. **Figure 8**a shows the charge and discharge profiles of the Si/LM/N-rGO composite electrode during the initial 3 cycles at a charge-discharge current of 250 mAg^{-1}. The composite electrode delivered initial specific discharge and charge capacities of 2697 and 1800 $mAhg^{-1}$ respectively, based on the combined active mass of Si and LM, with an initial coulombic efficiency (CE) of 62%. Figure 8b shows the performance of the Si electrode during

electrochemical cycling. The specific capacity of the Si control electrode drops from 1794 to 182 $mAhg^{-1}$ after 50 cycles indicating very rapid capacity decay, retaining a reversible capacity of only ~13%. In contrast, the Si/LM/N-rGO composite electrode retained a specific capacity of ~500 $mAhg^{-1}$ over 150 cycles with an excellent coulombic efficiency of ~100% after 140 cycles. The improved electrochemical performance of the composite electrode can be attributed to the enhanced structural stability and electrical conductivity obtained by the LM particles which bridge the cracks created during electrochemical cycling of Si.

The rate capability of the composite electrode was also investigated at higher charge-discharge current densities varying from 300 mAg^{-1} to 6000 mAg^{-1} (Figure 8c). The Si/LM/N-rGO electrode delivered specific capacities of 1223, 1052, 731, 321 and 111 mAg^{-1} at current densities of 300, 600, 1500, 3000 and 6000 $mAhg^{-1}$, respectively. Once the current rate was brought back to 300 from 6000 mAg^{-1} the composite electrode achieved a specific capacity of 1100 $mAhg^{-1}$ indicating excellent structural stability. This total recovery in performance can be attributed to the conductive network created by LM particles which contribute to healing the cracks formed in Si during electrochemical cycling.

3. Conclusion

We have developed Si/liquid metal thin films and Si/liquid metal/N doped rGO anodes to improve the electrical conductivity of a Si electrode during electrochemical cycling. For both systems, liquid metal particles demonstrate the capability of healing the cracks created in Si due to large volume expansion during lithiation and delithiation cycles, thereby, improving the electrical connectivity of Si after cracking. The Si/liquid metal/N doped rGO composite electrode demonstrated a better performance than pristine Si electrode and a discharge capacity of ~500 $mAhg^{-1}$ is retained after 150 cycles with a coulombic efficiency of ~100%. In addition, enhanced mechanical flexibility is observed in the Si/liquid metal/N doped rGO composite electrodes, which improves the system stability. We believe these results may

provide a new way to prepare high capacity anodes with improved electrochemical and mechanical performance.

4. Experimental Section

Fabrication of Si/LM thin films: Two types of electrodes were used in this study to evaluate the ability of LM in enhancing the structural stability and electrochemical performance of Si electrodes. First, Si thin film electrodes prepared by physical vapor deposition (PVD) were investigated to obtain an initial understanding on how liquid metal can improve the electrical connectivity of Si during lithiation and delithiation. The main advantage of this approach is that we can clearly monitor the direct impact of LM on the Si electrode since there are no other filler materials such as conductive additives or binders present in Si thin film electrodes. DC and RF magnetron sputtering techniques (Kurt J. Lesker PVD75 system) were used to synthesize Si thin films required for this study. Stainless steel substrates were first ground using 1200 grit silicon carbide paper and then polished by 1 micron diamond compound nap cloth. A high purity Ti target (99.995%) was used to deposit a Ti layer (~25nm), using DC magnetron sputtering at a power of 100 W and a pressure of 10 mTorr. Deposition of the Si thin film (200 nm) was conducted on top of the Ti layer using RF magnetron sputtering with an undoped Si target at 60 W and 4 mTorr. Pre-sputtering for 5 mins was conducted to remove any surface contamination present in the source targets. The substrate holder was allowed to rotate at 20 rpm during the deposition process to maintain uniformity of the films. To prepare Si/LM thin films, first, large galinstan droplets were subjected to ultra sonication in absolute ethanol to split them into micro-nano sized particles. 30 mg of galinstan (Sigma-Aldrich) was sonicated in 10 ml of absolute ethanol for 30 minutes in a sonication bath (B2500R-MTH) and drop casted onto the as deposited Si thin films inside an Ar filled glovebox to avoid oxidation of LM.

Synthesis of Si/LM/N-rGO composite: It has been reported previously that rGO in composite electrodes can accommodate large volume variations of Si during lithiation and delithiation owing to its superior flexibility.[32,40-42] Therefore, N-doped reduced graphene oxide (N-rGO) was added to the composite, to improve the structural stability of the electrode by holding the Si and LM particles in a 3D hierarchical matrix. Bulk LM was first sonicated in 1 mM ethanolic thiols (C12) to form micro-nano sized LM particles. The presence of C12 not only prevents small LM particles from re-assembling into large particles but also inhibits oxidation of LM during ultra-sonication.[43] 40 mg of galinstan was sonicated in 5 ml of Dodecanethiol (C12) ethanol solution (1 mM) for 30 minutes. 20 ml of absolute ethanol was added to 200 mg of Si nano particles (Sigma-Aldrich <100 nm) and sonicated for 2 hours in a sonication bath. Then the LM and Si solutions were mixed together and sonicated to obtain a homogeneous dispersion. N-doped graphene oxide was added to the above mixture to improve the structural stability of the active material as reported in previous studies.[28] 80 mg of N-doped reduced graphene oxide was sonicated separately in 5 ml of ethanol resulting in a dispersion which was then added to the Si/LM solution and mixed vigorously under sonication. (N-doped reduced graphene oxide was prepared as reported elsewhere. [44,45]) The resulting solution was dried at 50 °C under vacuum overnight and the Si/LM/N-rGO active material powder was then collected.

Structural and electrochemical characterization: Powder X-ray diffraction patterns were acquired using a Rigaku SmartLab diffractometer (Cu source). Surface morphology and elemental mapping of electrodes were characterized by scanning electron microscopy (Zeiss Sigma VP field emission scanning electron microscope equipped with an Oxford Xmax 50 Silicon drift EDS detector for X ray mapping). Nanoindentation tests were performed using the TI 950 Triboindenter (Hysitron Inc.), with a diamond Berkovich indenter tip. Si working electrodes were prepared by mixing 70 wt.% active material with 20 wt.% Super P as a conductive additive and 10 wt.% polyvinylidene fluoride as a binder in N-methyl-2-

pyrrolidone solvent. The slurry was casted onto a 14 μm thick copper foil using a doctor blade apparatus (Hohsen Co.) and dried under vacuum at 80 °C overnight. Coin-type cells (CR2032) were assembled in an Ar filled glovebox (O2 ≤ 0.1 ppm; H2O ≤ 0.1 ppm) using active material electrodes (Si thin films on stainless steel substrates and slurry coated composites on copper foil) as the working electrode, Li metal foil as the counter electrode, a 25 μm thick 2325 Celgard separator membrane and 1.0 M LiPF6 in ethylene carbonate/diethyl carbonate (LP40, BASF) = 50/50 (v/v) as the electrolyte. Galvanostatic charge-discharge tests were conducted over a voltage range of 0.01-2.0 V vs Li/Li^+ at charge-discharge currents ranging from 90 to 6000 mAg^{-1}. Cyclic voltammetry was performed on half coin cells at a scanning rate of 0.1 mVs-1 in a voltage window of 0.01-1.5 V vs Li/Li^+. Electrochemical impedance spectroscopy (EIS) measurements were carried out on half coin cells in the frequency range of 1 MHz to 10 mHz with an AC voltage of 5 mV amplitude. Electrochemical measurements were performed using a Biologic VMP300 Galvanostat/Potentiostat.

Acknowledgements

Characterization data for this study were obtained at the Central Analytical Research Facility (CARF) which is operated by the Institute for Future Environments (QUT). Access to CARF is funded by the Science and Engineering Faculty (QUT). SH would like to acknowledge QUT for the financial support given by QUTPRA scholarship. The financial support from ARC Discovery Projects (DP150101717 and DP180102003) is appreciated.

References

[1] J. Wang, T. Xu, X. Huang, H. Li, T. Ma, *RSC Adv.* **2016**, *6*, 87778.

[2] H. Kim, E.-J. Lee, Y.-K. Sun, *Mater. Today* **2014**, *17*, 285.

[3] N. Mahmood, T. Tang, Y. Hou, *Advanced Energy Materials* **2016**, *6*, 1600374.

[4] H. Jin, C. Guo, X. Liu, J. Liu, A. Vasileff, Y. Jiao, Y. Zheng, S.-Z. Qiao, *Chem. Rev.* **2018**.

[5] M. Ashuri, Q. He, L. L. Shaw, *Nanoscale* **2016**, *8*, 74.

[6] M. A. Rahman, G. Song, A. I. Bhatt, Y. C. Wong, C. Wen, *Adv. Funct. Mater.* **2016**, *26*, 647.

[7] X. Lu, W. Suqing, L. Guoxue, D. Liangxing, L. Dongdong, W. Haihui, Q. Shizhang, *Small* **2016**, *12*, 853.

[8] H. Liu, D. Su, G. Wang, S. Z. Qiao, *J. Mater. Chem.* **2012**, *22*, 17437.

[9] W.-J. Zhang, *J. Power Sources* **2011**, *196*, 13.

[10] Z.-L. Xu, X. Liu, Y. Luo, L. Zhou, J.-K. Kim, *Prog. Mater Sci.* **2017**, *90*, 1.

[11] J. Ryu, D. Hong, H.-W. Lee, S. Park, *Nano Research* **2017**, *10*, 3970.

[12] J. Ryu, T. Bok, S. Kim, S. Park, *ChemNanoMat* **2018**, *4*, 319.

[13] M. Gu, Y. He, J. Zheng, C. Wang, *Nano Energy* **2015**, *17*, 366.

[14] J.-Y. Li, Q. Xu, G. Li, Y.-X. Yin, L.-J. Wan, Y.-G. Guo, *Mater. Chem. Front.* **2017**, *1*, 1691.

[15] L. Ji, Z. Lin, M. Alcoutlabi, X. Zhang, *Energy & Environmental Science* **2011**, *4*, 2682.

[16] N. Nitta, G. Yushin, *Particle & Particle Systems Characterization* **2014**, *31*, 317.

[17] Y. Sun, N. Liu, Y. Cui, *Nature Energy* **2016**, *1*, 16071.

[18] J. Graetz, C. C. Ahn, R. Yazami, B. Fultz, *Electrochem. Solid-State Lett.* **2003**, *6*, A194.

[19] Q. Xu, J.-Y. Li, J.-K. Sun, Y.-X. Yin, L.-J. Wan, Y.-G. Guo, *Advanced Energy Materials* **2017**, *7*, 1601481.

[20] R. Yi, J. Zai, F. Dai, M. L. Gordin, D. Wang, *Nano Energy* **2014**, *6*, 211.

[21] Z. Luo, D. Fan, X. Liu, H. Mao, C. Yao, Z. Deng, *J. Power Sources* **2009**, *189*, 16.

[22] N. Liu, Z. Lu, J. Zhao, M. T. McDowell, H. W. Lee, W. Zhao, Y. Cui, *Nat Nanotechnol* **2014**, *9*, 187.

[23] N. Kim, C. Oh, J. Kim, J.-S. Kim, E. D. Jeong, J.-S. Bae, T. E. Hong, J. K. Lee, *J. Electrochem. Soc.* **2017**, *164*, A6075.

[24] C. Wang, H. Wu, Z. Chen, M. T. McDowell, Y. Cui, Z. Bao, *Nature Chemistry* **2013**, *5*, 1042.

[25] F.-S. Li, Y.-S. Wu, J. Chou, M. Winter, N.-L. Wu, *Adv. Mater.* **2015**, *27*, 130.

[26] B. Li, F. Yao, J. J. Bae, J. Chang, M. R. Zamfir, D. T. Le, D. T. Pham, H. Yue, Y. H. Lee, *Sci Rep* **2015**, *5*, 7659.

[27] N. Nitta, F. Wu, J. T. Lee, G. Yushin, *Mater. Today* **2015**, *18*, 252.

[28] Y. Wu, L. Huang, X. Huang, X. Guo, D. Liu, D. Zheng, X. Zhang, R. Ren, D. Qu, J. Chen, *Energy & Environmental Science* **2017**, *10*, 1854.

[29] K. C. Wasalathilake, D. G. D. Galpaya, G. A. Ayoko, C. Yan, *Carbon* **2018**, *137*, 282.

[30] M. Zhou, T. Cai, F. Pu, H. Chen, Z. Wang, H. Zhang, S. Guan, *ACS Applied Materials & Interfaces* **2013**, *5*, 3449.

[31] F. Maroni, R. Raccichini, A. Birrozzi, G. Carbonari, R. Tossici, F. Croce, R. Marassi, F. Nobili, *J. Power Sources* **2014**, *269*, 873.

[32] H. Tang, J.-p. Tu, X.-y. Liu, Y.-j. Zhang, S. Huang, W.-z. Li, X.-l. Wang, C.-d. Gu, *Journal of Materials Chemistry A* **2014**, *2*, 5834.

[33] F. Hoshyargar, J. Crawford, A. P. O'Mullane, *J. Am. Chem. Soc.* **2017**, *139*, 1464.

[34] M. Shafiei, F. Hoshyargar, N. Motta, A. P. O'Mullane, *Materials & Design* **2017**, *122*, 288.

[35] Y. Yang, N. Sun, Z. Wen, P. Cheng, H. Zheng, H. Shao, Y. Xia, C. Chen, H. Lan, X. Xie, C. Zhou, J. Zhong, X. Sun, S.-T. Lee, *ACS Nano* **2018**, *12*, 2027.

[36] H. Li, X. Zhu, H. Sitinamaluwa, K. Wasalathilake, L. Xu, S. Zhang, C. Yan, *J. Alloys Compd.* **2017**, *714*, 425.

[37] J. Xie, L. Tong, L. Su, Y. Xu, L. Wang, Y. Wang, *J. Power Sources* **2017**, *342*, 529.

[38] X. Zhou, Y.-X. Yin, A.-M. Cao, L.-J. Wan, Y.-G. Guo, *ACS Applied Materials & Interfaces* **2012**, *4*, 2824.

[39] W.-H. Ho, C.-F. Li, H.-C. Liu, S.-K. Yen, *J. Power Sources* **2008**, *175*, 897.

[40] H.-C. Tao, L.-Z. Fan, Y. Mei, X. Qu, *Electrochem. Commun.* **2011**, *13*, 1332.

[41] S.-H. Park, H.-K. Kim, D.-J. Ahn, S.-I. Lee, K. C. Roh, K.-B. Kim, *Electrochem. Commun.* **2013**, *34*, 117.

[42] H. Xiang, K. Zhang, G. Ji, J. Y. Lee, C. Zou, X. Chen, J. Wu, *Carbon* **2011**, *49*, 1787.

[43] J. N. Hohman, M. Kim, G. A. Wadsworth, H. R. Bednar, J. Jiang, M. A. LeThai, P. S. Weiss, *Nano Lett.* **2011**, *11*, 5104.

[44] D. C. Marcano, D. V. Kosynkin, J. M. Berlin, A. Sinitskii, Z. Sun, A. Slesarev, L. B. Alemany, W. Lu, J. M. Tour, *ACS Nano* **2010**, *4*, 4806.

[45] L. Sun, L. Wang, C. Tian, T. Tan, Y. Xie, K. Shi, M. Li, H. Fu, *RSC Advances* **2012**, *2*, 4498.

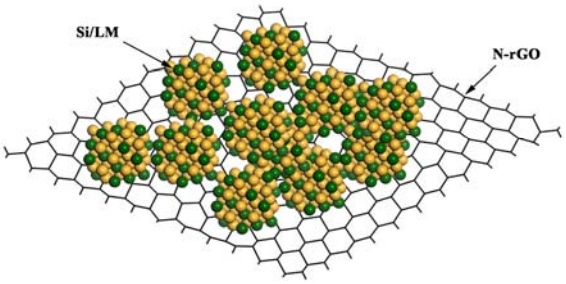

Figure 1. Schematic illustration of Si/LM embedded in N-rGO matrix.

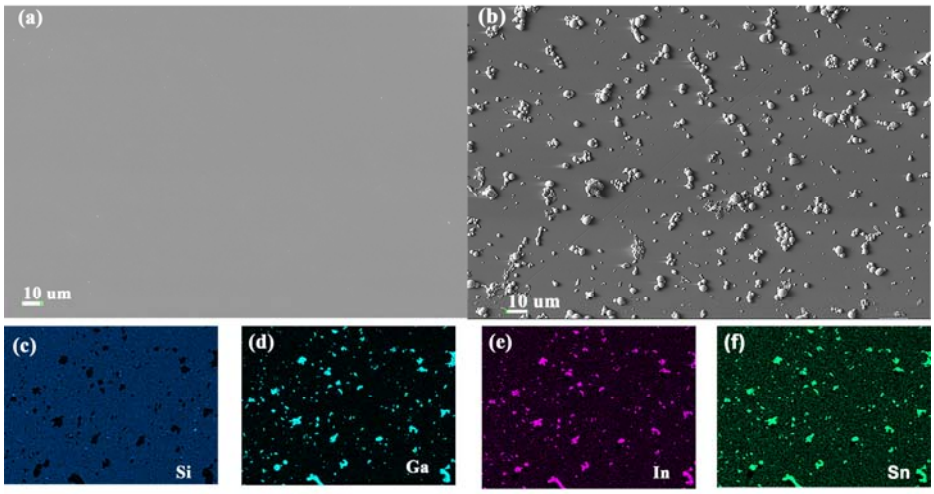

Figure 2. SEM image of (a) PVD deposited Si thin film, (b) LM drop casted Si thin film and (c-f) EDS elemental mapping of LM on Si thin film.

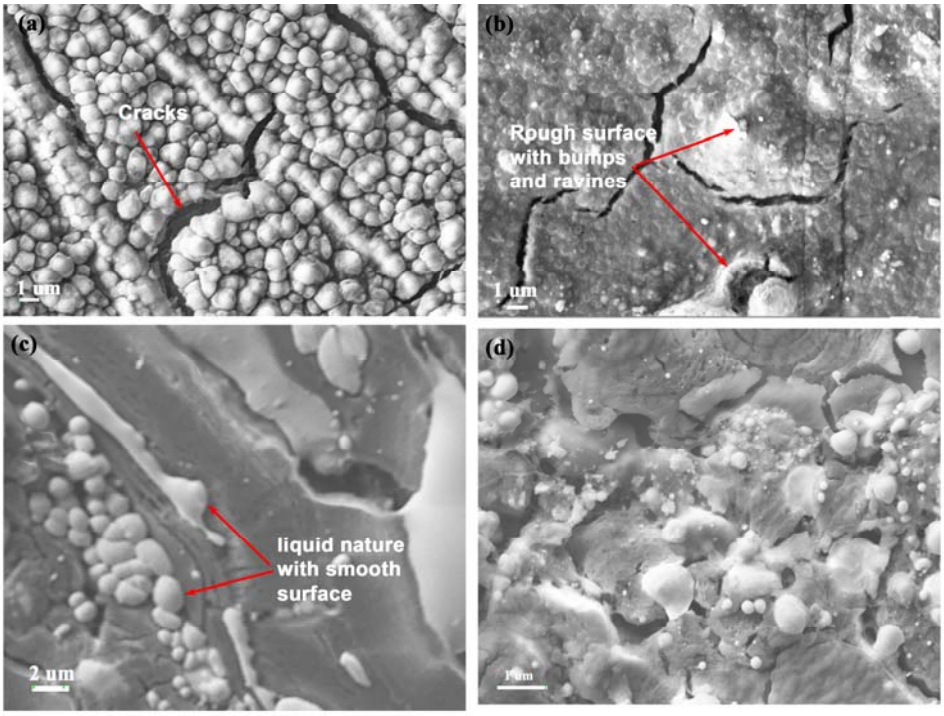

Figure 3. SEM images of (a) Si electrode, (b) LM deposited Si thin film after lithiation, (c,d) LM deposited Si thin film after delithiation.

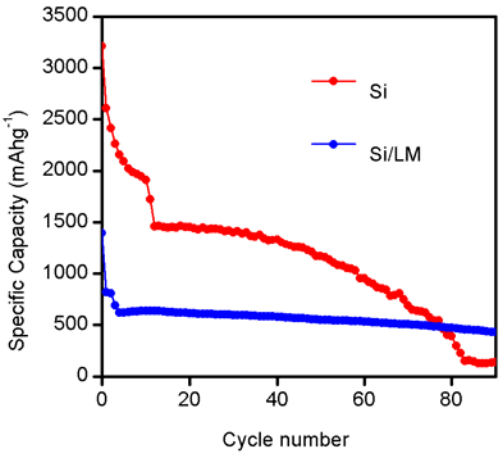

Figure 4. Cycling performance of Si and Si/LM thin films.

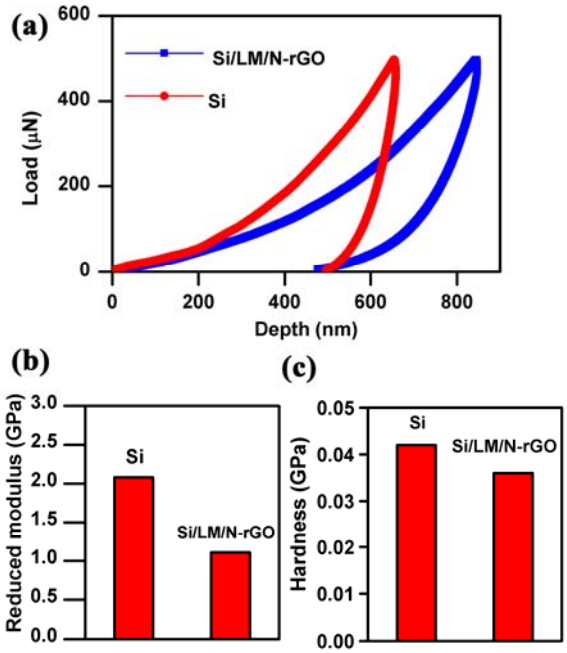

Figure 5. (a) Load-displacement curves of Si and Si/LM/N-rGO electrodes (b) reduced modulus and (c) hardness obtained from nanoindentation tests.

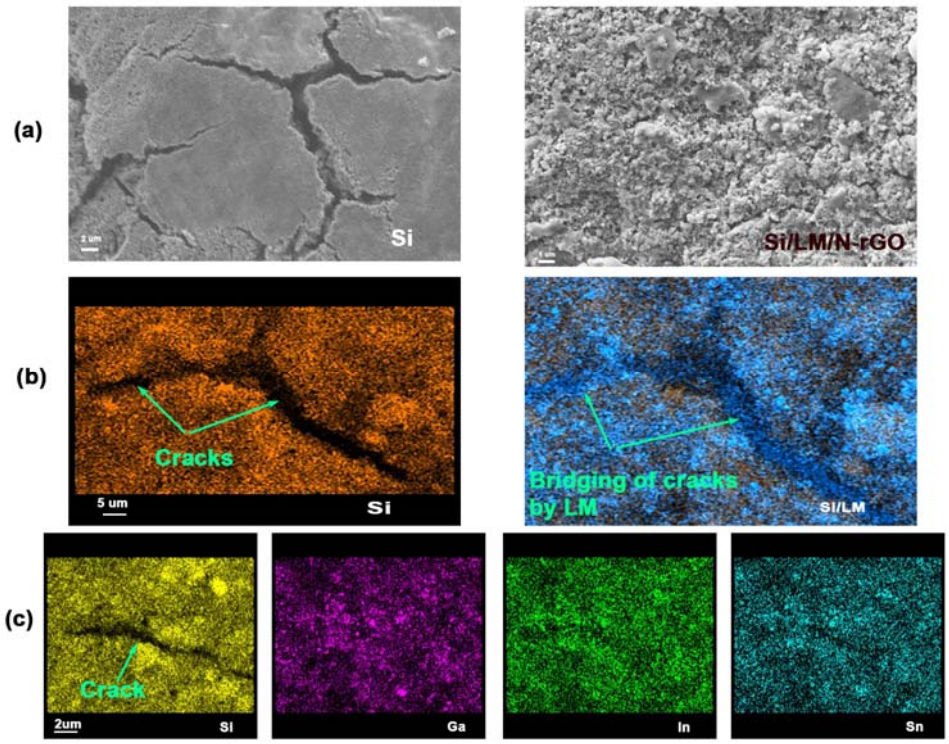

Figure 6. (a) SEM images of Si and Si/LM/N-rGO, (b) EDS image showing the ability of LM bridging the gaps in Si/LM/N-rGO and (c) EDS element mapping of the Si/LM/N-rGO electrode after 3 cycles.

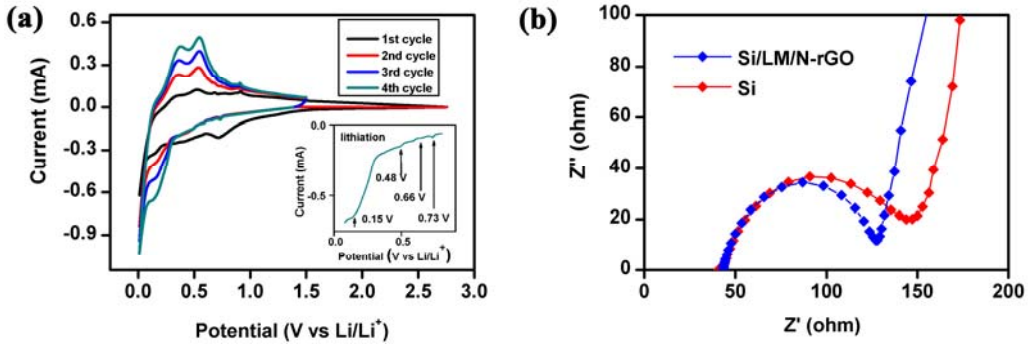

Figure 7. (a) Cyclic voltammograms of the Si/LM/N-rGO composite electrode for first four cycles obtained at a scan rate of 0.1 mVs^{-1}, (b) Nyquist plot of control-Si and Si/LM/N-rGO composite electrodes before galvanostatic cycling.

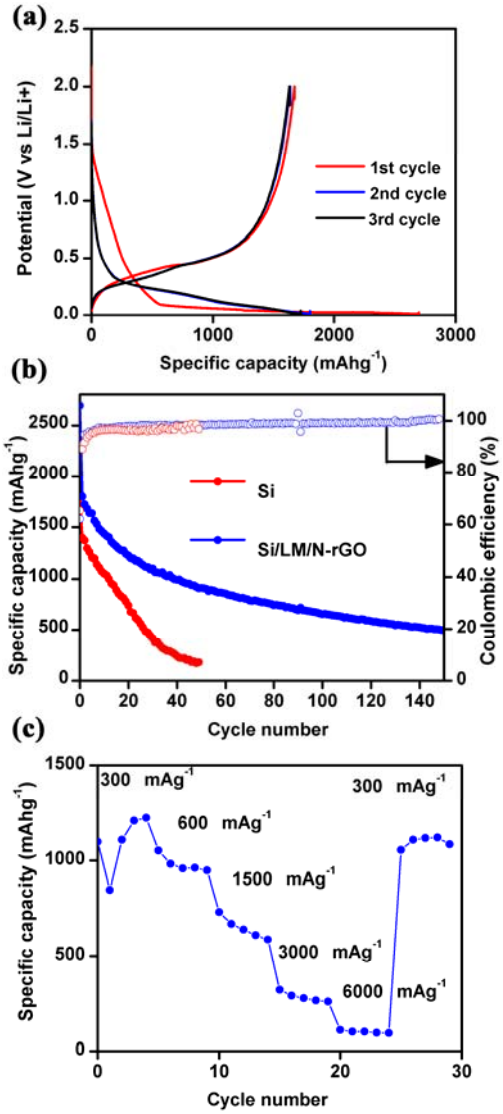

Figure 8. (a) Galvanostatic discharge-charge profiles of the Si/LM/N-rGO composite electrode during the first 3 cycles at a current density of 0.1 C, (b) Comparison of cyclability and coulombic efficiency of Si and Si/LM/N-rGO composite electrodes cycled at a current density of 0.1 C, (c) Rate capability of the Si/LM/N-rGO composite electrode.